Invited Paper

Advanced Integration Schemes for High-Functionality/High-Performance Photonic Integrated Circuits

James W. Raring, Matthew N. Sysak, Anna Tauke-Pedretti, Mathew Dummer, Erik J. Skogen, Jonathon S. Barton, S. P. DenBaars, and Larry A. Coldren

Materials and Electrical and Computer Engineering Depts.,
University of California, Santa Barbara, 93106
jraring@engineering.ucsb.edu

ABSTRACT

The evolution of optical communication systems has facilitated the required bandwidth to meet the increasing data rate demands. However, as the peripheral technologies have progressed to meet the requirements of advanced systems, an abundance of viable solutions and products have emerged. The finite market for these products will inevitably force a paradigm shift upon the communications industry. Monolithic integration is a key technology that will facilitate this shift as it will provide solutions at low cost with reduced power dissipation and foot-print in the form of highly-functional optical components based on photonic integrated circuits (PICs). In this manuscript, we discuss the advantages, potential applications, and challenges of photonic integration. After a brief overview of various integration techniques, we present our novel approaches to increase the performance of the individual components comprising highly functional PICs.

Keywords: Semiconductor lasers, semiconductor optical amplifiers, electroabsorption modulators, metalorganic chemical vapor deposition, photodetectors, wavelength-division multiplexing.

1 INTRODUCTION

TERAHERTZ carrier frequencies characteristic of lightwave communication systems have enabled the necessary bandwidth to meet the increasing demand for higher data rates. Furthermore, optical communication systems in the 1.30µm to 1.55µm wavelength range offer desired low dispersion and loss characteristics allowing for high-bit-rate long-distance transmission with reduced repeater spacing over that of electrical coaxial lines[1]. The finite market in the telecommunications industry coupled with an abundance of chip vendors offering unique solutions creates intense competition[2]. The prevailing technology in this competition will not only fulfill the required performance specifications for the application, but will also be low cost and possess additional desired characteristics such as a compact foot print and low power consumption. Monolithic integration of optoelectronic components is the answer to this challenge. The generation, detection, modulation, switching, and transport of light on chip not only enables cost reduction, but also allows for a new generation of high functionality photonic integrated circuits (PICs) with reduced size and power dissipation.

The majority of optoelectronic components comprising modern day communications systems are discrete in nature. Several of these discrete components with differing functions are then interconnected using fiber splices in a configuration to provide the required system functionality. The underlying advantage of this method is that each component is optimized for one specific function, enabling deployment of state of the art components. However, there are several shortcomings involved with this method. The difficulty in efficiently coupling light on and off each discrete chip is great. Advances in the coupling between the semiconductor chip and optical fiber using mode converters is a significant step in reducing the coupling loss, yet coupling is still a dominant source of optical loss. Another draw back

Nanophotonic Packaging, edited by Allen M. Earman, Ray T. Chen,
Proc. of SPIE Vol. 6126, 61260H, (2006) · 0277-786X/06/$15 · doi: 10.1117/12.655999

to discrete components is the expense involved with packaging each component individually. This is the major expense as devices are taken from fabrication to deployment. A reduction of the packaging cost can be accomplished by using co-packaging of optoelectronic components although device-to-device coupling is still an issue.

The monolithic integration of the optoelectronic devices on a single chip offers the potential to completely eliminate the device-to-device coupling problem. This can provide a significant reduction in packaging cost and package size as well as increased reliability and reduced power dissipation. Increased reliability results from the elimination of possible mechanical movements amongst the elements of an optical train and the reduced driving currents allowed by the reduction in optical coupling loss between elements. The reduction in required drive currents subsequently results in decreased device power consumption.

1.1 The Challenge of Monolithic Integration

There are several examples of high functionality PICs where multiple active components are placed on a common chip. Widely-tunable transmitters, photocurrent driven wavelength converters (PD-WC), and transceivers are three such examples, as these devices will facilitate enabling technologies in wavelength division multiplexing (WDM) applications such as dynamic provisioning, reconfigurable optical add/drop multiplexers (ROADMs), wavelength routing, and optical packet switching[3]. The latter two devices require the monolithic integration of widely tunable light sources such as the sampled-grating DBR laser (SG-DBR) with modulators, semiconductor optical amplifiers (SOA), and photodiodes.

The widely-tunable electroabsorption modulator (EAM) based PD-WC making using of a receiver ridge parallel to a transmitter ridge is a viable architecture for single chip wavelength conversion[3,4]. The PD-WC is a particularly challenging device since the individual components comprising the PIC necessitate unique waveguide architectures for optimum performance. Low threshold, high efficiency lasers require high optical confinement QW active region architecture for maximized modal gain[5]. Integrated QW EAMs utilizing the quantum confined stark effect (QCSE) for high efficiency, necessitate a QW band-edge that is blue-shifted from that of the laser or SOA operation wavelength for reasonable insertion loss/extinction properties. State of the art SOAs employ measures for reduced photon density in gain region such as low optical confinement QWs, so high saturation powers can be achieved[6]. Finally, high performance photodiodes employ a bulk absorber region and can make use of unique waveguide or internal structure design for high photocurrent/high speed operation[7]. The unique characteristics required by each component for optimum performance clearly poses significant difficulty in realizing a high performance single-chip wavelength converter.

1.2 Guidelines for Monolithic Integration

There are some general requirements that must be fulfilled when monolithically integrating optoelectronic components. First, each integrated component must function as intended. The performance of each integrated component must operate at a level that will enable the PIC as a whole to achieve its specified performance level. Clearly, as these levels are increased, the performance demands of the individual integrated components will also be increased. The second requirement is that the operation of one component must not adversely effect the operation of another. That is, each component should be isolated from the other components on chip and function as if it were discrete. These requirements allow for the design of PICs using an optoelectronic building blocks approach such that discrete components sharing a common growth and processing platform can be combined in a way that creates a higher functionality device or PIC. When implementing a method for monolithic integration, the trade-off between fabrication difficulty and device optimization capabilities should be carefully weighed since added processing steps and growth complexity can lead to increased manufacturing costs and yield reduction. Additionally, the method should not be prohibitively time consuming or expensive. A review of some of some integration methods are given in the following section.

2 INTEGRATION TECHNOLOGIES

When selecting the appropriate integration method for the specific device, the strengths and weaknesses of the candidate methods should be carefully considered with the understanding that the design flexibility of the integration scheme must be increased as the PIC functionality and performance demands are increased. The butt-joint regrowth method is an example of an integration scheme offering a high degree of versatility[8]. This method involves the selective removal of the as-grown waveguide/MQW region followed by the non-planar selective regrowth of waveguide/MQW material with the desired band edge and waveguide architecture. The butt-joint regrowth process, depicted in Fig. 1a, is highly-flexible as it enables the use of a centered QW (c-MQW) active region for maximized modal gain and allows each integrated component to possess a unique band edge or waveguide architecture. Once all desired structures are realized on chip with the butt-joint method, an additional regrowth is performed for the upper cladding. This technique allows for a high degree of separate optimization of the individual components within the PIC. However, the difficulty associated with matching thickness and achieving the desired composition to avoid reflection and loss at the interface is great[8]. Furthermore, the complexity of this process is compounded as the number of desired band edges and waveguide architectures is increased since each will require an additional regrowth.

Selective area growth (SAG) has been shown to be useful in providing multiple band edges across the wafer in a single growth step[9]. In this method a dielectric mask is patterned on the wafer, which is then subjected to MOCVD growth. Growth is limited to regions between the dielectric mask, where thickness and composition of the growing layers are modified based on the adjacent mask pattern. Following the selective growth, the dielectric mask is removed and an additional regrowth is performed for the upper cladding. A schematic diagram illustrating this method is shown in Fig. 1b. This technique provides the capability to realize c-MQW active regions for maximized modal gain and QW EAMs on the single chip with a single growth. However, since this technique exploits the contrast in surface kinetics of the growth constituents on the semiconductor and dielectric, a high degree of calibration/optimization is required to tightly control the reactor conditions. Surface diffusion lengths limit the abruptness of the transition region, which may be on the order of tens of microns. Additionally, the optical mode overlap with the MQW may not be ideal in all sections due to the thickness variation.

An established and very simple integration platform is based on the use of offset QWs, where the multi-quantum well (MQW) active region is grown above a passive bulk waveguide. This allows for the selective etching of the MQW in regions where gain is not required, leaving the non-absorbing waveguide. Once the active and passive regions have been defined, the upper cladding is regrown[10]. A schematic of this method is shown in Fig. 1c. Although this is a relatively simple process and does not add significant processing steps in the case of the widely-tunable SG-DBR laser, it allows for only two band edges on a single chip, one from the MQW and one from the waveguide. Not only is the modal gain in the offset QW design less than optimal since the peak of the optical mode is offset from the QWs, but also when integrating an EAM with the SG-DBR laser the trade off between loss, tuning, and absorption may lead to reduced performance of one or more components. Furthermore, this scheme forces the use bulk Franz Keldysh (FK) type EAMs,

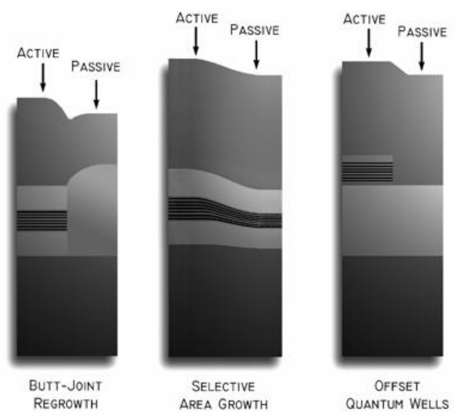

(a) (b) (c)

Fig. 1. Various techniques for achieving active and passive sections orthogonal to the growth direction.

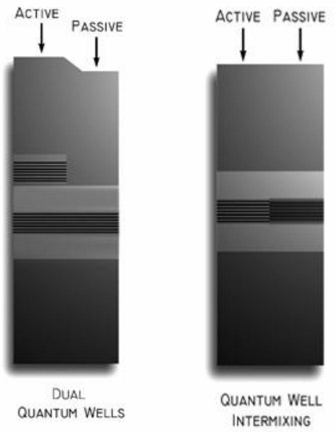

(a) (b)

Fig. 2. Foundational integration techniques explored in this work for enhanced high-functionality PIC performance

which are not as efficient as QW EAMs based on the Quantum Confined Stark Effect (QCSE)[11].

3 BACKGROUND: INTEGRATION FOUNDATIONS

Although there has been some great success in producing PICs based on the various methods discussed above, these fabrication schemes require a significantly increased level of growth complexity as the PIC functionality is elevated. These techniques rely on butt-joint regrowth or SAG to realize blue-shifted QWs on the same chip as a laser for use in an EAM. Furthermore, aside from the butt-joint method, these schemes provide little flexibility in the cross-sectional waveguide architectures. This has limited the performance of previous single-chip EAM-based PD-WCs since they were fabricated using the offset QW platform in which inefficient FK type EAMs were employed[3]. In other work, it was the common QW stack used in the laser, SOA, and photodetector, that ultimately limiting the linearity of the receiver and hence the overall device performance[4]. Thus a key challenge of the PIC designer has been to allocate the trade-offs in such a way that the overall performance of the device is sufficient for the intended application. With this, there is clearly a demand for integration solutions that provide greater design flexibility without significant increase in fabrication complexity.

3.1 Dual QW Platform for Integrated QW EAM

Electroabsorption modulators can greatly benefit from the presence of QWs in the absorption region since the QCSE can be exploited to enable higher absorption efficiency and lower insertion losses[11]. However, as mentioned above, achieving multiple QW band edges on the same chip for the integration of a QW EAM with a laser often includes added growth/processing complexities, which makes simple solutions offering these characteristics attractive. The simple offset QW method discussed above has been used with great success in fabricating various integrated structures: SG-DBR lasers with integrated EAMs[12], SG-DBR lasers with integrated semiconductor optical amplifiers (SOAs)[13], SG-DBR lasers with integrated Mach-Zehnder modulators[14], optical receivers[15], and wavelength converters[3,16]. However, in addition to the non-optimal modal gain, the main drawback of the offset QW method is the limitation of each integrated component to one of two band edges, the active QWs or the bulk waveguide. Thus, this scheme does not allow for the flexibility necessary for the fabrication of PICs requiring multiple QW bandedges for use in lasers and EAMs.

In recent progress we have demonstrated the capability to realize a second MQW band-edge on chip using the same simple processing scheme employed in the offset QW method. This is accomplished by growing an MQW centered within the bulk waveguide below the offset MQW. The waveguide MQW is blue shifted from the bandedge of the active offset QWs to be used in gain regions. Since the resulting structure contains two stacks of QWs, this scheme is called the dual QW platform and is depicted in Fig. 2a. With only a moderate increase in the base structure growth complexity, QW EAMs can now be realized on the same chip as widely-tunable lasers using the identical simple processing steps as in the offset QW method. This scheme offers a large degree of EAM design freedom since the MQW design can be tailored without disruption of the laser active region. This freedom opens new avenues for the use of specially designed wells for optimum modulator performance in terms of well depth, well/barrier width, and well symmetry.

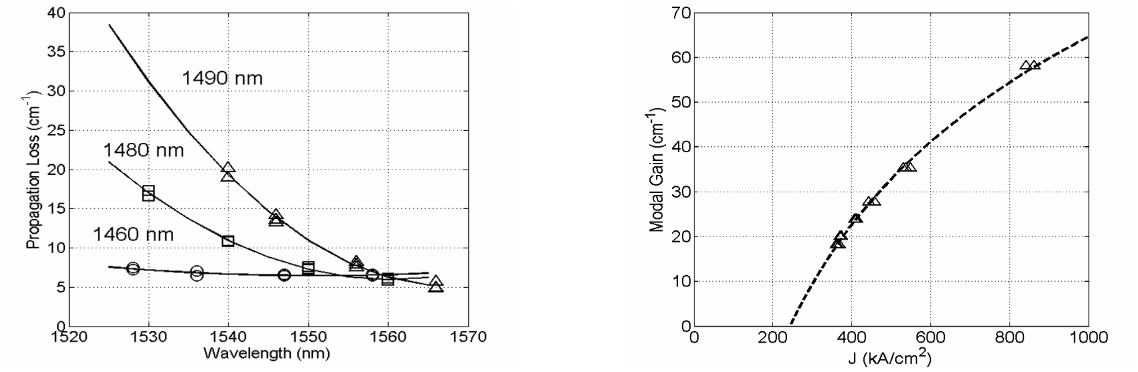

(a) (b)

Fig. 3. (a) Propagation loss versus operating wavelength for three different waveguide MQW designs employed in the dual QW platform. (b) Two parameter fit of modal gain versus current density for broad area lasers fabricated from dual QW design with a waveguide MQW PL peak placed at 1480 nm demonstrating a transparency current of 270 kA/cm^2 and material gain parameter of 764 cm^{-1}.

Furthermore, for the bulk FK EAMs, relatively high waveguide doping levels (~2E17 cm^{-3}) have been incorporated in the past to achieve large peak electric fields in order to maximize device efficiency. This is not conducive to high speed operation due to the large associated capacitance associated with the structure. For the dual QW platform, it is actually detrimental to performance to have high waveguide doping levels. Since doping that is above the QW active region will lower the electric field, and reduce the device efficiency. As a result, the doping in the waveguide portion of the structure has been lowered significantly (5E16 cm^{-3}). This allows for lower EAM capacitance and hence higher bandwidths along with enhanced EAM efficiency when compared with the more traditional offset QW EAMs.

To maintain high device output powers, it is critical that the unbiased absorption edge of the MQW centered in the waveguide not provide unreasonable amounts of loss since these QWs will be present throughout all passive components and mirror sections in addition to the EAMs. The propagation loss versus wavelength was measured for different waveguide MQW designs possessing photoluminescence (PL) peaks of 1460nm, 1480nm, and 1490nm using an integrated tunable laser and passive photocurrent taps placed at various propagation distances. The results of this study, shown in Fig. 3a, demonstrate the trade-off in passive loss versus decreasing absorption edge of the EAM wells, which results in high EAM absorption efficiencies. From this data, the design employing waveguide QWs with a PL peak of 1480nm was used for PIC fabrication as the propagation loss across the full optical communication C-Band remains below 17 cm^{-1} and is not unreasonable for the applications discussed in this work. The epitaxial base structure of this design used a standard active offset MQW with seven 6.5 nm compressively strained QWs and eight 8.0 nm barriers with a peak photoluminescence wavelength of 1550nm. The MQW centered within the waveguide consisted of seven 9.0 nm compressively strained wells and six 5.0 nm tensile strained barriers. As shown in Fig. 3a, the loss

A necessary characterstic of the dual QW platform is that the presence of the QWs in the waveguide not hinder carrier transport to the offset MQW used in the laser active regions and/or SOAs. More specifically, electrons must now traverse the waveguide MQW before arriving at the offset MQW for recombination with injected holes. Fabry Perot (FP) broad area laser (BAL) devices were fabricated using the dual QW platform and were subjected to pulse testing. The inverse differential efficiency versus FP laser length was plotted to extract the injection efficiency and modal loss. The injection efficiency was found to be 73% and the modal loss was found to be ~6 cm^{-1}, which are both in close correlation to the 73-76% injection efficiency and ~6cm^{-1} loss observed for BAL devices fabricated on the standard offset QW platform. By using a two parameter fit to plot the BAL device modal gain versus current density as shown in Fig. 3b, a transparency current density of 270 kA/cm^2 and material gain parameter of 764 cm^{-1} was extracted. The close correlation of all material properties extracted from dual QW BALs with those previously extracted from BAL devices fabricated using the standard offset QW platform demonstrates efficient electron transport through the waveguide wells and into the offset wells.

3.2 Quantum Well Intermixing for Centered Quantum Well Active Regions and Integrated QW EAM

Another method to realize multiple QW bandedges is through quantum well intermixing (QWI), which allows for the strategic, post growth, tuning of the QW band edge using a relatively simple procedure. As this technique enables the employment of centered MQW active regions for maximized modal gain lasers and blue shifted QWs for use in EAMs, QWI breaks the trade-off associated with the simple fabrication scheme offered by the offset QW method and the design flexibilities offered by butt-joint regrowth and SAG. QWI makes use of the metastable nature of the compositional gradient found at heterointerfaces. The natural tendency for materials to interdiffuse is the basis for the intermixing process. Also, because QWI does not change the average composition, but only slightly changes the compositional profile, there is a negligible index discontinuity at the interface between adjacent sections. This eliminates parasitic reflections that can degrade performance.

There are several methods to accomplish QWI[17,18,19]. In this work we employ the implant-enhanced interdiffusion technique, which relies on the diffusion of point defects created during an ion implantation into an InP implant buffer layer grown above the MQW active region. This method has been shown to have good spatial resolution, and be controllable using anneal time, temperature, and implant dose[5]. Furthermore, we have developed a method to further control the QWI process by achieving any number of QW band edges in the structure using selective removal of the catalyst. This method requires a single ion implant followed by a rapid thermal anneal step. The extent of intermixing is precisely controlled using the anneal time. Once the desired band edge is reached for a given region, the anneal is stopped and the point defects are removed in that region by selective removal of the InP implant buffer layer. The anneal is then continued until the desired band edge in another section is reached, at which point the point defects are removed in this section. The process, illustrated in Fig. 4a, can be repeated to achieve any number of band edges across the wafer as demonstrated in Fig. 4b with a plot of photoluminescence peak versus anneal time for samples with and without implantation and samples with the implant buffer layer removed.

Several aspects of the QWI material are crucial for the successful operation of PICs incorporating SG-DBR lasers and QW EAMs and required characterization. The loss in the passive and mirror regions must be made low such that high device output powers can be achieved. To characterize the loss properties of intermixed material, active/passive buried ridge stripe (BRS) Fabry-Perot (FP) with different magnitudes of photoluminescence shift were pulse tested using the cleave back method. The FP laser devices possessed an active length of 500 μm and an initial passive waveguide length of 2500 μm, The passive region loss was plotted as a function of photoluminescence peak wavelength at an operation wavelength of 1570nm, as shown in Fig. 5a. An exponential curve provides a good fit with the data. As evident from the figure, the passive region modal loss is strongly dependent on the relative position of the intermixed band edge.

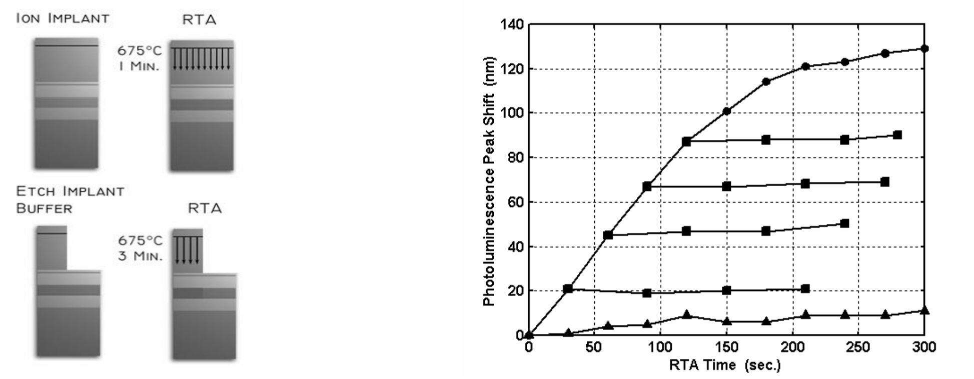

(a) (b)

Fig. 4. (a) Schematic of the intermixing process. From left to right on top; ion implantation followed by rapid thermal annealing. From left to right on bottom; selective removal of vacancy point defects required for blue-shifting, followed by an additional anneal (b) Peak photoluminescence peak shift as a function of anneal time, showing the initial linear increase in the peak shift and the complete halting of the peak shift for samples for which the implant buffer layer has been etched. Symbols indicate nonimplanted (triangles), implanted (circles), and samples with partial anneal followed by the removal of the implant buffer layer (squares).

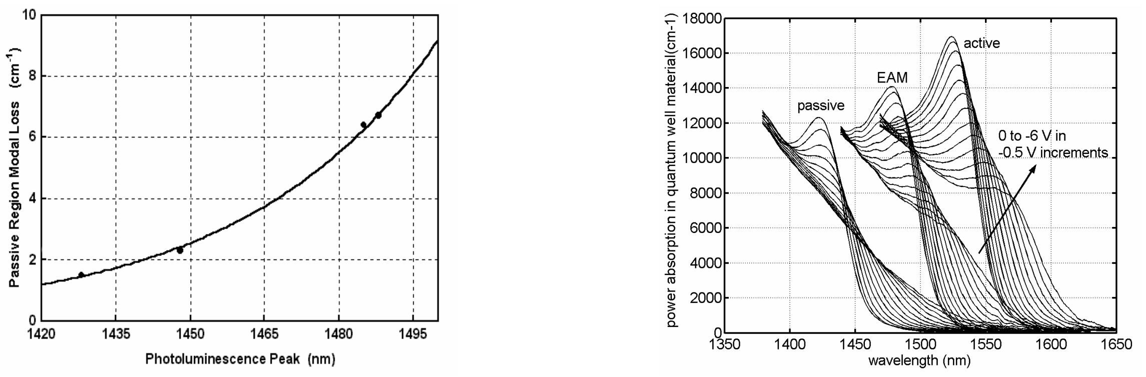

(a) (b)

Fig. 5. (a) Passive region modal loss as a function of photoluminescence peak wavelength at a wavelength of 1570nm. Solid line indicates an exponential curve fit, while symbols indicate modal loss data extracted from active/passive lasers. (b) Power absorption vs. wavelength measured using photocurrent spectroscopy for as-grown and two regions whose quantum wells are intermixed to different levels.

Maximizing the magnitude of intermixing can minimize the modal loss in the passive region.

As mentioned in the introduction, QW EAMs are desirable over bulk FK EAMs due to performance enhancement resulting from the QCSE, which gives rise to a strong exciton peak in the material absorption spectrum and can result in low and even negative chirp behavior in an EAM[20]. Thus for the realization of an optimum EAM, it is crucial that the QWI process does not severely degrade the absorption characteristics of the as-grown material. This effect was studied using photocurrent spectroscopy on diodes fabricated with as-grown (λ_{pl} = 1537) and material intermixed to two levels (λ_{pl} = 1483 and λ_{pl} = 1429) at bias levels from 0 to -6 V in -0.5 V increments. The results of this study are shown in Fig. 5b. The devices used in this study contained seven 6.5 nm compressively strained QWs and eight 8.0 nm barriers placed between two 120 nm bulk waveguides. The effect of QWI on the exciton peak is made clear by comparison of the band edges for the as-grown and intermixed regions of the photodiodes. As the degree of intermixing increases, and the exciton peaks shift to shorter wavelengths, the exciton magnitude decays. With increased intermixing, the exciton peaks also decay more rapidly as a function of applied bias voltage. Although there is some degree of exciton degradation with intermixing, the exciton remains the dominant characteristic of the absorption spectra, especially for intermixing levels required for EAM employment.

This method of QWI has been further qualified through the successful fabrication of short-cavity distributed Bragg reflector (DBR) lasers with integrated EAMs[21], widely-tunable multi-section sampled-grating (SG) DBR lasers with integrated EAMs[22], and chip-scale wavelength converters[4,23]. A detailed review of these devices fabricated using our QWI method along with a thorough description of the fabrication process can be found elsewehere[24].

4 CHALLENGES OF INCREASED FUNCTIONALITY PIC

Although both of the foundational integration technologies discussed above enable the use of QWs in the EAM regions and QWI provides maximized modal gain in the lasers, significant limitations are imposed as higher PIC functionality is required. This is a result of the limited waveguide architecture options for use in the integrated components. In the case of the widely-tunable EAM based PD-WC, the integration of SOAs and photodetectors with the SG-DBR laser and EAM is required. When employing the simple yet versatile dual quantum well or QWI schemes for device fabrication, the SOA gain region must make use of the same MQW active region as used in the laser. Since these components have different functionalities, it is clear that they will also require different considerations when designing the MQW active region.

High modal gain is desired in the laser such that low threshold currents, high wall plug efficiency, and high output powers can be achieved. The threshold modal gain (Γg_{th}) is governed by Eq. 1, where Γ is the optical confinement factor, g_{th} is the threshold material gain, α_i is the optical loss in the cavity, and α_m is the mirror loss. From Eq. 1 it is clearly advantageous to maximize the optical confinement factor within the laser to achieve high modal gain. The output saturation power, P_{OS}, defined as the output power at which the gain drops by 3 dB, is a critical consideration in SOA design. The output saturation power can be approximated by Eq. 2[25] , where G_o is the unsaturated gain, w is the width of the gain region, d is the thickness of the gain region, a is the differential gain of the material, τ is the carrier lifetime, and again Γ is the optical confinement factor. From Eq. 2, it is clear that for the realization of high saturation power SOAs, a low optical confinement factor is desirable. Thus, there is clear performance trade-off between the integrated laser and SOA imposed by the optical confinement properties of the device architecture.

Since the core component of the PICs discussed in this work is the widely-tunable SG-DBR laser, the first design consideration of the MQW active region must be given to the laser performance. Thus, the confinement factors in the base structure MQW active regions are designed to be relatively high at ~6% and ~9.5% for seven active QWs employed in the dual QW and QWI platforms, respectively. Without modifications for enhanced SOA performance, the saturation power of the SOAs is expected to be on the order of 11-13 dBm at current densities in the range of 10 kA/cm^2.

$$\Gamma g_{th} = \alpha_i + \alpha_m \qquad Eq.1 \qquad\qquad P_{os} = \left(\frac{G_o Ln(2)}{G_o - 2}\right)\left(\frac{wd\,h\nu}{a\Gamma\tau}\right) \qquad Eq.\,2$$

Another limitation imposed on highly functional PICs such as the PD-WC when using the dual quantum well or QWI integration platforms pertains to photodetectors. In the dual QW platform, the photodetector absorption region must utilize either the offset MQW used in the laser or the higher energy bandedge centered MQW used in the EAMs and passive components as shown in Fig. 2b. In the QWI platform, the photodetector is forced to use the centered MQW with any of the available bandedges rendered with QWI. In both cases, the best choice is the as-grown active QWs, since these wells have the lowest energy absorption edge resulting in the highest absorption coefficient and least wavelength dependence. Since this structure sandwiches intrinsic QWs between the p and n-type cladding layers, the resulting photodetector structure is classified as a p-i-n photodiode which employs QWs in the absorbing medium. While the active QWs are the best available option on these platforms, they are definitely not the optimum choice for use in a photodetector. The reasons for this are threefold: The potential barriers introduced by the QWs in the absorbing region hinder carrier escape, which results in premature saturation properties. The high confinement factor leads to a steep exponential absorption profile that results in a front-end-concentrated current density, again leading to saturation. Finally, since the thickness of the intrinsic region is set by the MQW active region design, the PIC designer has little freedom to tailor the electric field strength and profile in the photodetectors. Conventional p-i-n photodiodes operating in the 1.55 μm range employ a bulk absorber such as InGaAs with a lower energy bandgap than that of the operating wavelength to avoid complications associated with QWs and minimize wavelength dependent absorption properties. More advanced devices employ special architectures such as evanescently coupled waveguide schemes to create a uniform absorption profile along the detector and minimize front-end saturation[26]. In the following sections we will explore techniques to improve integrated SOA and photodetector performance.

5 TECHNIQUES FOR ENHANCED PIC PERFORMANCE

5.1 2-Dimensional Solutions: Flared Waveguide

By inspection of Eq. 2, it is clear that there are several possible approaches to increasing the saturation power within an SOA. Reduction of the carrier lifetime and/or differential gain through the use of a differing gain material such as quantum dots or through higher current density operation would both be beneficial to the SOA performance[27]. Another approach would be to reduce the photon density over the gain medium, which can be accomplished by reducing the optical confinement factor or by increasing the cross-sectional area of the active region to expand the optical mode[28]. Perhaps the latter of the two options would be the simplest method to increase the saturation power. When increasing the cross-sectional area of the active region, one has the option to increase the thickness (d) and/or the width (w) of the gain material in the active region. However, in typical waveguide configurations such as the surface-ridge architecture, an increase in thickness of the active material also leads to an increase in the confinement factor and is actually detrimental to the saturation power. However, the optical confinement factor is relatively insensitive to the waveguide width, such that the width can be increased without significant increase in confinement factor. Furthermore, the width of the waveguide is simply controlled with the lithographic mask design such that waveguide flares can be implemented without any increase in fabrication or growth complexity.

In order to study the saturation power benefits offered by simple waveguide flares, photoreceivers consisting of SOAs and QW p-i-n detectors with various waveguide flare/taper schemes were fabricated using the offset QW process[15]. The SOAs were designed as two-stage amplifiers. The first stage uses 200-µm-long by 3-µm-wide waveguide to provide unsaturated gain for low input powers while keeping amplified spontaneous emission noise to a minimum. The second stage employs a linearly flared waveguide from 3 µm to between 6 µm and 12 µm. Curved and flared input waveguides were used for reduced parasitic reflections. The devices were soldered to Cu blocks for continuous wave (CW) testing at an input wavelength of 1548nm in the TE polarization state. A scanning electron micrograph of the photoreceivers is shown in Fig. 6a.

The output power at which the gain rolls off by 1dB is plotted versus input power at a current density of 8.3 kA/cm^2 for the different SOA designs in Fig. 6b. From this plot it is seen that the 1dB compression point can be increased from the 10-11 dBm range with no flare to nearly 16 dBm at a final flare width of 12 µm. The result is a 3-4X increase in power handling capabilities of the SOA through the use of simple waveguide flares. Furthermore, as shown by the plot of device gain versus length in Fig 7a, with the proper choice of device length, the SOA gain can be on the order of 20 dB.

The saturation point of a photodetector can be classified by the photocurrent density at which the power out versus power in response compresses by a specified value. With this in mind, the goal was to improve the performance of QW p-i-n type photodetectors such that the offset active MQW could be employed in the photodetector regions with sufficient performance. The QW p-i-n detectors provide high absorption coefficients due to the high modal confinement and material absorption associated with the waveguide structure and QWs, respectively. These properties coupled with the characteristic exponential absorption profile in the detector results in a majority of the photocurrent generated in the front-end. While this allows for short detector lengths it also causes front end photodetector saturation. This saturation is evident in the degradation of small signal bandwidth with increased photocurrent densities. Since wider waveguides result in lower current densities for a fixed input power, the saturation power of a photodetector can be increased with the use of wide waveguides. As mentioned above, this is attractive since it requires only changes to the lithographic mask design and no processing or growth deviations are necessary. However, the effects of having a larger device area increases the capacitance and in turn decreases the bandwidth. Therefore, the best bandwidth versus increased saturation power trade-off is a waveguide scheme in which the width is tapered from large to small. In order to study the potential benefits of such schemes, three detector designs were fabricated on the same chip as the SOAs and tested. The first detector design had a length of 150-µm with a straight 3-µm-wide ridge. The first 50 µm of the detector employed bulk waveguide material (passive material) as the absorber followed by 100 µm of offset MQW active material. The second

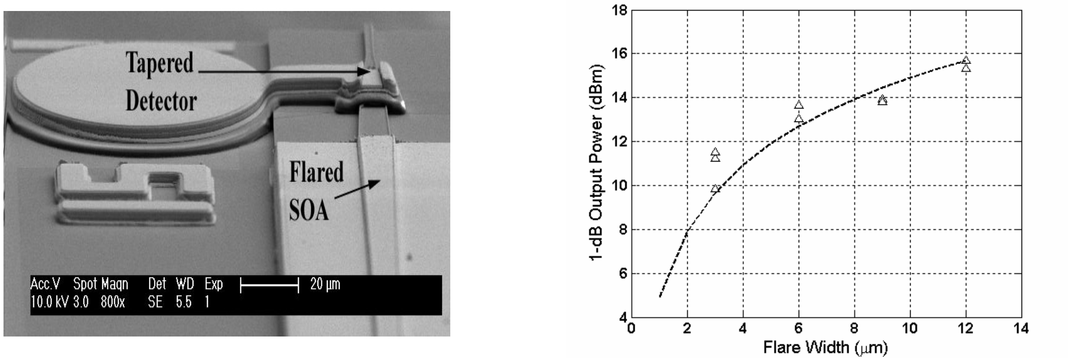

(a) (b)

Fig. 6 (a) SEM of photoreceiver employing flared/tapered waveguides for improved saturation performance. (b) 1dB compression point of output power as a function of final flare width for SOA operating at 8.3 kA/cm^2.

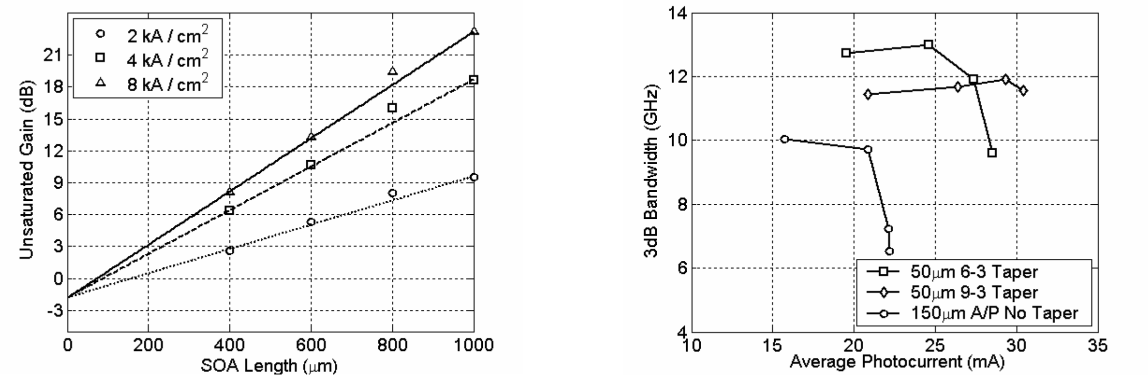

(a) (b)

Fig. 7. (a) Unsaturated gain versus SOA length for various operation current densities and (b) 3dB photodetector bandwidth versus average photocurrent for various taper schemes demonstrating the benefits from widening the front-end waveguide width of the photodetector.

and third designs were 50-μm in length and used a linear ridge taper from 6 μm to 3 μm and 9 μm to 3 μm, respectively.

In Fig. 7b, the small-signal 3dB bandwidths versus average photocurrent are plotted for the different detector designs at a reverse bias of 4V using a termination load of 50Ω. The key aspect of this plot is not the magnitude of the unsaturated bandwidth since the total diode area and hence capacitance of the various designs are different, but rather the photocurrent at which the bandwidth begins rolling off. The 3 μm wide non-tapered device demonstrates bandwidth degradation at ~20mA of average photocurrent. However, the tapered designs do not begin degrading until photocurrent levels of >25mA and >30mA for the 6 μm and 9 μm wide front-ends, respectively. Thus, through the use of simple waveguide tapers, the saturation power levels was increased by 50% in a photodetector with 2/3 the total diode area.

5.2 3-Dimensional Solutions: QWI and MOCVD Regrowth

In the previous section, we presented recent progress in which significant improvements to SOA and photodetector performance were made through simple waveguide flares. Although this technique is elegant in that it does not require any additional processing or growth steps for the integration of these components with SG-DBR lasers and EAMs, the possible performance improvements are limited. In the case of the SOA, simply increasing the width can reduce the heat dissipation efficiency due to the device aspect ratio. Since gain and saturation power are dependent on the operation current density and it is this current density generating heat, insufficient heat dissipation can lower the optimum operation current density and hence degrade performance. This effect counteracts the benefits of decreased photon density provided by the flares.

State of the art high saturation power SOAs employ a drastically different gain region design than the MQW designs employed in the SG-DBR lasers of this work. These gain region schemes include quantum dots, low optical confinement (LOC) QW active regions, or slab coupled optical waveguide architectures. The LOC configuration is an attractive choice since the photon density within the QWs can be kept relatively low. Using the LOC-QW scheme, impressive saturation powers of +23 dBm and +28 dBm have recently been demonstrated[6,28].

The photocurrent handling capabilities of the QW p-i-n type photodetector is intrinsically limited for three reasons. Saturation in a p-i-n photodetector can be explained by the classic space charge effect, which is a result of the slow escape time of holes from the absorbing layer[7]. The spatial distribution of photogenerated carriers in the absorbing medium effectively reduces the applied electric field due to screening effects. Once the field drops below a critical value, the holes can no longer maintain their saturation velocity and the power in versus power out response of the device begins to roll-off. Furthermore, the presence of quantum wells in the absorbing region introduces potential barriers, which impede carrier escape and hence compound the saturation issue[29]. The third issue, front-end saturation, can be dealt with by evanescent coupling schemes or simple waveguide flares as discussed above[15,26].

The uni-traveling carrier (UTC) photodiode has been designed specifically to circumvent the influence of hole transport on the performance of the detector by making the total charge transit time heavily dominated by electrons. The active layers of the UTC are the neutral InGaAs:Zn absorption layer and the adjacent depleted wide bandgap InP electron collection layer. Under normal operation of the photodiode, carriers are photogenerated in the absorber layer. The minority carriers, electrons, diffuse towards the collector layer where they accelerate to their overshoot velocity and drift across the collector layer. The escape time of the majority carriers, holes, from the absorption layer is negligible since it is set by their dielectric relaxation time[7]. Since the overshoot velocity of electrons is an order of magnitude higher than the saturation velocity of holes, the UTC can achieve saturation current densities 4-6 times higher than that in p-i-n photodiodes[7].

With the above discussion, the intrinsic difficulties of achieving high performance SOAs and photodetectors integrated with SG-DBR lasers and QW EAMs on the dual QW quantum or 2-dimensional QWI platform should be clear. In order for PICs to compete with their discrete counterparts, the necessity for a break-through technology that will circumvent these trade-offs is essential. This technology is further exploitation of QWI. By using QWI to render the as-grown c-MQW passive and then performing straightforward, blanket MOCVD regrowth, state of the art SOA and photodetector architectures can be integrated.

The proposed novel integration procedure is initially identical to that of the 2-dimensional single regrowth QWI process for the realization of multiple c-MQW band-edges to be employed in the laser, EAM, and passive sections[5]. However, upon removal of the InP buffer layer and 1.3Q stop etch layers, a blanket MOCVD regrowth is performed for the growth of a thin InP:Si layer followed by a 1.3Q:Si stop etch layer, an InP:Si confinement tuning layer (CTL), an offset low-confinement MQW (o-MQW) SOA gain region with similar compositions and thicknesses to that of the standard c-MQW active region sandwiched between 25nm barriers, 50nm InP, and a 200nm InP:Zn cap layer. Since the CTL layer functions to remove the active wells from the peak of the optical mode, the choice of the thickness is a key aspect in the design and will be discussed in detail below. The proof of concept and key growth aspects were previously reported[30,31]. Following the regrowth, the sample is patterned with Si_xN_y and a wet chemical selective etch process is carried out such that the o-MQW structures remain in regions where low optical confinement active regions are desired with intermixed c-MQW regions below. A second blanket MOCVD regrowth for the realization of UTC photodiode structures is performed. Again, the regrowth initiates with a thin InP:Si regrowth layer and a 1.3Q:Si stop etch layer, but is then followed by the growth of the InP collector, conduction band smoothing layers, the InGaAs:Zn absorber layer, and a 150nm InP:Zn cap layer. The thickness and doping of both the collector and absorber layers have a great impact on the expected device performance and will be discussed further below. The epitaxial structure of the UTC was based largely off of the structure employed by Ishibashi et al[7]. The sample is then patterned with Si_xN_y and a wet etch is performed such that the UTC structure remains only where detectors are desired. A final blanket MOCVD regrowth is performed to grow the p-type InP:Zn cladding and p-contact InGaAs:Zn layers to yield four distinct regions remain on a single chip: The as-grown c-MQW active regions to be used for high gain lasers and SOA sections, the partially intermixed c-MQW regions for use in high efficiency QW-EAMs, low confinement o-MQW regions grown above intermixed wells for high saturation power SOAs, and finally UTC structures grown over intermixed wells for high-saturation power high-bandwidth photodiodes. A complete and labeled schematic of the resulting regions on a single chip is shown in Fig. 8.

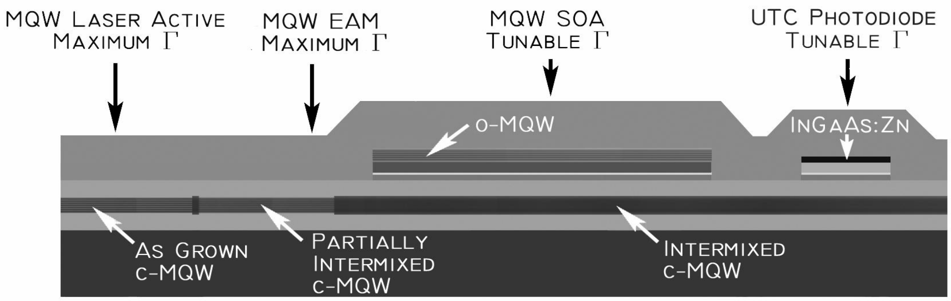

Fig. 8. Side-view schematic of QWI and MOCVD regrowth integration scheme enabling the integration of high gain lasers, QW EAMs, high saturation power amplifiers, and high saturation power photodetectors.

In Fig. 9a, a schematic side-view of the SOA is presented. By growing the o-MQW active region above the intermixed c-MQW, the active wells are taken off the peak of the optical mode and hence the confinement factor is reduced. A finite difference technique was used to solve the wave equation and compute the optical confinement within the active QWs for both the c-MQW and o-MQW regions. The base structure consists of ten 6.5 nm compressively strained QWs and eleven 8.0 nm barriers sandwiched between two 1050 nm waveguide layers. The refractive index and simulated optical modes are plotted in Fig. 9b for the c-MQW and Fig. 9c for an o-MQW consisting of five wells with a CTL thickness of 150nm. To show how the optical confinement in the o-MQW is influenced by the CTL thickness and number of offset QWs, the finite difference technique was used to solve for the optical confinement as a function of the CTL thickness for three different numbers of offset QWs. The simulation, shown in Fig. 10a, assumes a ridge waveguide architecture with a ridge width of 5µm. According to the simulations, confinement factors in the vicinity of 1% can be achieved.

The saturation power and chip gain can be predicted using Eq. 2 and material gain data from previous BAL devices, respectively. These simulations are shown in Fig. 10b, which plots chip saturation power and chip gain versus CTL thickness for 3-5 offset QWs. The simulations assume a current density of 2.5 kA/cm^2/well, a radiative recombination coefficient of $B = 0.3\times10^{-10}$ cm^3/s, an Auger recombination coefficient, $C = 6\times10^{-29}$ cm^6/s, and a device length of 1500µm. According to Fig. 10b, saturation powers >20dBm with chip gains in the 7-15 dB range can be simultaneously achieved for such a device with the proper choice of CTL thickness and number of offset QWs.

To demonstrate the viability of QWI plus offset QW growth for the realization of low confinement and high confinement active regions on the same chip, 3µm wide ridge type FP devices of both active region types were fabricated on the same chip. The o-MQW consisted of 5 QWs with a CTL thickness of 1450nm, yielding a confinement factor of ~1.5%. The cleave back method was used to plot the inverse differential efficiency versus FP laser length to extract the injection efficiency and optical loss of both active region types. The injection efficiency was found to be 70% and 73 % in the c-MQW and o-MQW active regions, respectively. The optical loss was found to be 20 cm^{-1} and 3 cm^{-1} in the c-MQW and o-MQW active regions, respectively. A two-parameter fit was used to plot the threshold modal gain

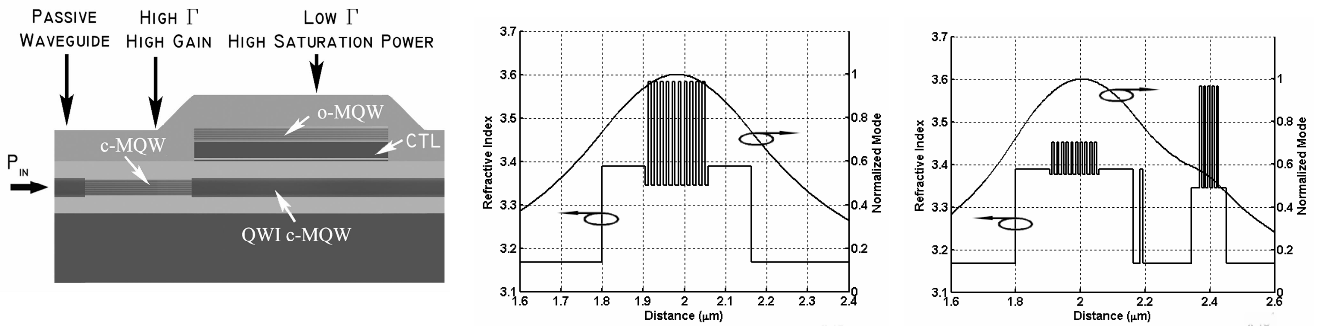

(a) (b) (c)

Fig. 9. (a) Side view schematic of SOA with high gain c-MQW section and high saturation power o-MQW section. In (b) and (c) the refractive index and mode profile are plotted versus waveguide position illustrating the drastic reduction in confinement factor that can be achieved in the o-MQW.

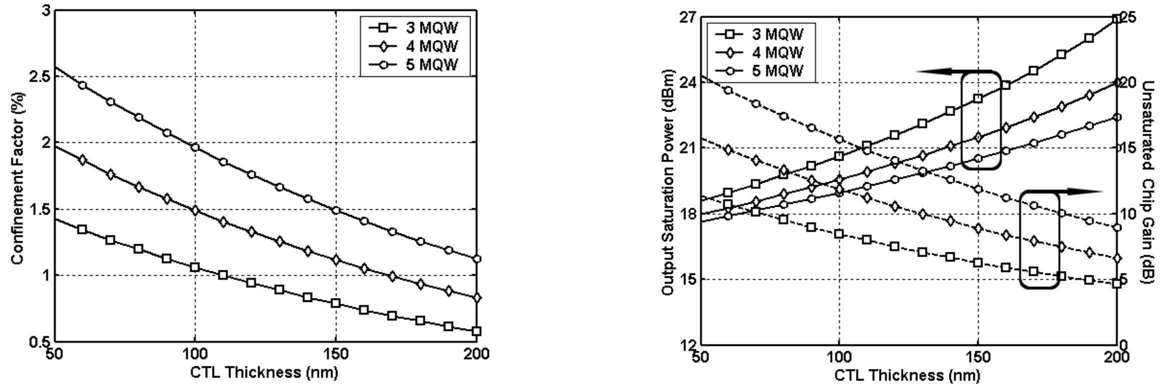

(a) (b)

Fig. 10. Simulated (a) optical confinement factor and (b) saturation power/ unsaturated chip gain versus CTL thickness in the o-MQW for 3, 4, and 5 offset QWs. The simulations assume a current density of 2.5 kA/cm^2/well, a radiative recombination coefficient of B = 0.3x10^{-10} cm^3/s, an Auger recombination coefficient, C = 6x10^{-29} cm^6/s, and a device length of 1500μm.

versus current density. The fit yielded a modal gain parameter of 94.1 cm^{-1} in the c-MQW active region and 9.1 cm^{-1} in the o-MQW active region, which is in good agreement with the simulated difference in optical confinement factor.

The separate growth for the realization of the UTC structure enables a high level of detector design freedom. However, the choice of the InGaAs:Zn absorber layer thickness and InP collector layer thickness is crucial. Since the integrated UTC photodetector of this work will use an edge-coupled architecture, the internal quantum efficiency is not largely dependent on the absorber thickness. Thus, we employ a thin 50nm absorber, such that the diffusion component of the electron transport does not dominate the total transport time. Since the collector layer functions to space the InGaAs:Zn absorber layer from the core waveguide consisting of an intermixed c-MQW, the choice of the collector thickness will influence the absorption profile and hence the internal quantum efficiency of the detector.

Beam propagation simulations were performed using commercially available software from Rsoft in order to predict the absorption profile. The simulated absorption profile for our integrated UTC structure with varying collector thicknesses along with that expected in a p-i-n detector formed from the as-grown c-MQW stack consisting of ten 6.5nm wells is shown in Fig. 12a. The loss values of 6800 cm^{-1} used for the InGaAs:Zn and 5000 cm^{-1} used for the p-i-n QWs was extracted experimentally with photocurrent spectroscopy. The three collector thicknesses used in the simulation were 150nm (squares), 200nm (triangles), and 250nm (circles) with an absorber thickness of 50nm. As shown in Fig. 11a, with proper design the absorption profile can be tuned in the UTC device to take on a more linear shape opposed to the fixed steep exponential profile exhibited by the QW-p-i-n. This feature of the integrated UTC structure enables the

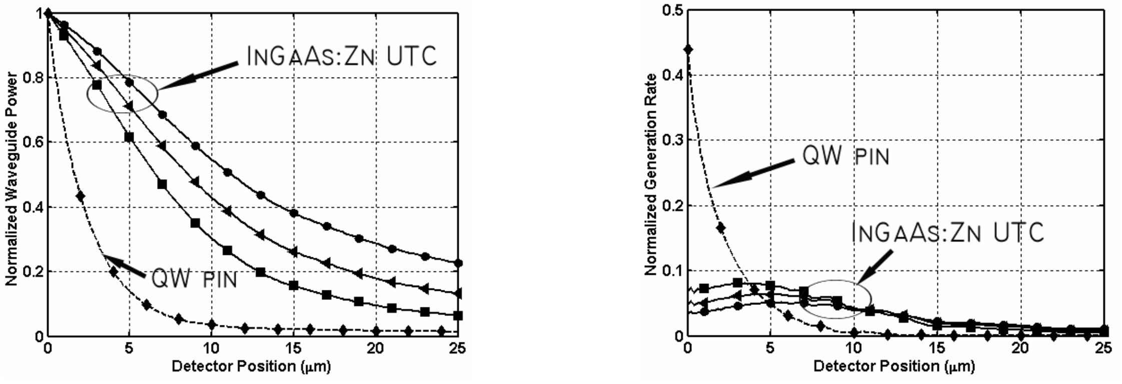

(a) (b)

Fig. 11 (a) Simulated waveguide power along photodetector for a QW p-i-n (dashed line) and UTC photodiodes (solid lines). The simulations use a 50nm thick absorber and collector thicknesses of 100nm (squares), 150nm (triangles), and 200nm (circles). (b) Simulated carrier generation rate along detector for a QW p-i-n (dashed line) and UTC photodiode (solid lines). The simulations use a 50nm thick absorber and collector thicknesses of 100nm (squares), 150nm (triangles), and 200nm (circles).

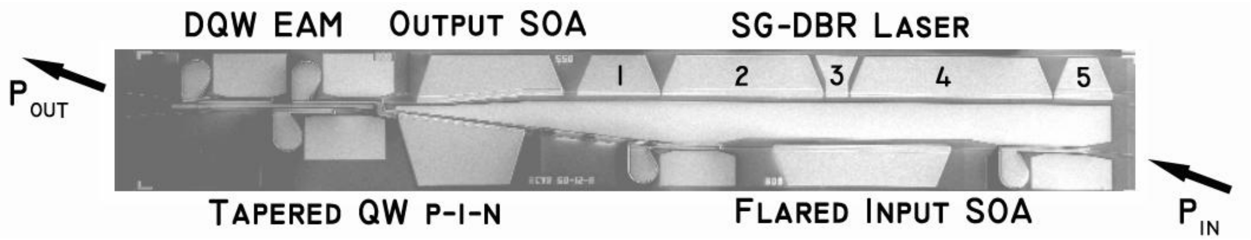

Fig. 12 Top view SEM of PD-WC device fabricated using the dual QW platform incorporating flared/tapered waveguide schemes for enhanced receiver performance.

control over the carrier generation profile since this profile is governed by the slope of the absorption profile. The normalized carrier generation rates along the detector lengths resulting from the absorption profiles are shown in Fig. 11b. The UTC type detectors demonstrate a radically more uniform generation rate along the length of the device than does the c-MQW p-i-n detector, with an ~8X reduction in front-end photocurrent generation. This implies that the front-end saturation characteristics plaguing traditional waveguide photodiodes can be avoided using the regrowth scheme. Since the collector layer also sets the detector capacitance as it is the intrinsic layer, careful consideration of the trade-off between bandwidth and desired absorption profile must be taken.

6 PIC RESULTS

In the following sections results are presented from PICs fabricated on the dual QW and on the QWI platform. First we report the performance 10 Gb/s widely-tunable transmitters monolithically integrated with photoreceivers employing waveguide flares for both the SOA and the detector for the realization of a 10 Gb/s PD-WC. In the following section results are shown for a 10 Gb/s widely-tunable negative-chirp transmitter fabricated using QWI. Finally, the results from SOAs and UTC photodiodes fabricated using the novel QWI and MOCVD regrowth scheme are presented.

6.1 Dual QW 10 Gb/s Transmitter with Integrated Receiver

In some of our most recent progress we have monolithically integrated SG-DBR lasers with QW EAMs and SOA/QW p-i-n receivers employing flares and tapers for improved saturation characteristics using the dual QW platform. This device, shown in Fig. 12, was the first single chip widely tunable EAM based 10 Gb/s PD-WC providing 10 dB of output signal extinction and a net conversion gain. Further details and performance characteristics of the PD-WC device can be found elsewhere[32]. Here we focus on the transmitter portion of the device which is comprised of a five section SG-DBR laser followed by an SOA for output amplification and a QW EAM consisting of seven 9.0 nm compressively strained wells and six 5.0 nm tensile strained barriers. The 5 sections of the SG-DBR laser are, from front to back of the laser: front mirror, gain, phase, rear mirror, and backside absorber, as depicted in Fig. 12. The phase and mirror sections function to tune the wavelength of the laser[10].

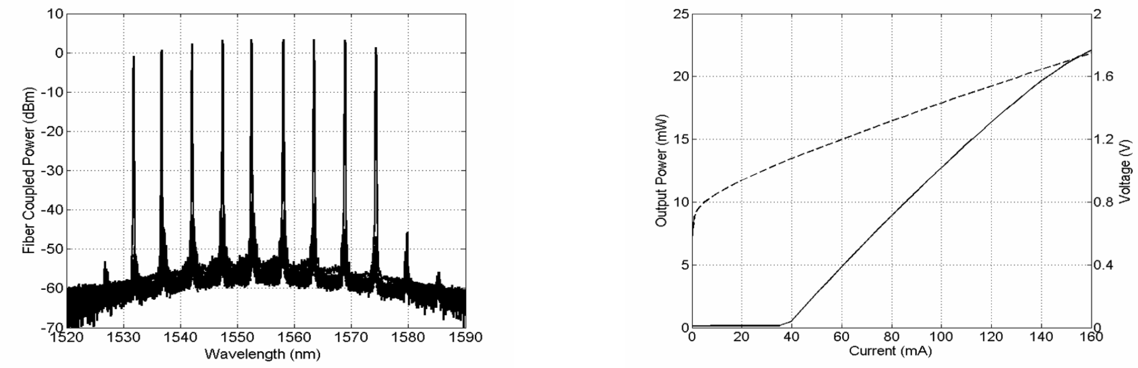

(a) (b)

Fig. 13. (a) Tuning spectra and (b) light/voltage characteristics versus current for SG-DBR fabricated on dual QW platform.

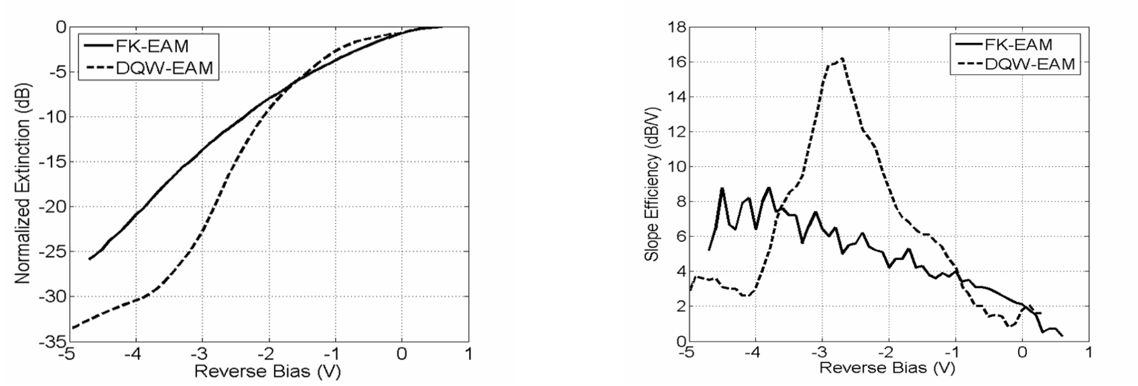

(a) (b)

Fig. 14 (a) Extinction and (b) slope efficiency versus reverse bias for 400µm long EAMs employing the FK absorption mechanism fabricated on the offset QW platform and employing the QCSE absorption mechanism fabricated using the dual QW platform.

The output tuning spectra of the transmitter, Fig. 13a, demonstrated over 40nm of continuous tuning with a side mode suppression ratio (SMSR) of > 35 dB at all wavelengths. The SG-DBR lasers demonstrated threshold currents of under 40mA with over 20 mW of output power at a gain current of 160 mA as shown in the plotted LIV of Fig. 13b. There is no significant degradation in the laser performance over that of SG-DBRs fabricated using the offset QW platform, and in fact, there is a slight enhancement in the tuning efficiency of the lasers due to the addition of the QWs in the waveguide.

The benefits offered by the dual QW platform over that of the standard offset QW can be clearly seen when comparing the efficiencies of 400µm long EAMs fabricated with each platform. In Fig. 14a, EAM extinction versus bias, and in Fig. 14b, EAM slope efficiency versus bias are presented for both bulk FK type EAMs fabricated using the offset QW method and QW EAMs fabricated using the dual QW method. The QW EAM provides up to 2.5X the efficiency than that of the FK device. Furthermore the QW EAM has an optimal operating bias regime in the 2.5 to 3.5V with respect to the extinction efficiency. The FK EAM demonstrates an increase in extinction efficiency with an increase in reverse bias. This indicates that in order to achieve maximum extinction efficiency in the EAM, high insertion losses will be suffered.

The reduced doping levels in the EAM required for optimized efficiency in the dual QW platform over that of the offset QW platform enables a significantly lowered device capacitance. In Fig. 15a, a plot of capacitance versus reverse bias is shown for 40 µm by 40µm capacitor structures fabricated from both bulk FK material and dual QW material. As can be seen from the figure, with the reduction in doping, the capacitance is decreased by a factor of 2 and depletes more rapidly with reverse bias in the QW EAM. The frequency response enhancement is shown in Fig. 15b, with a 400 µm

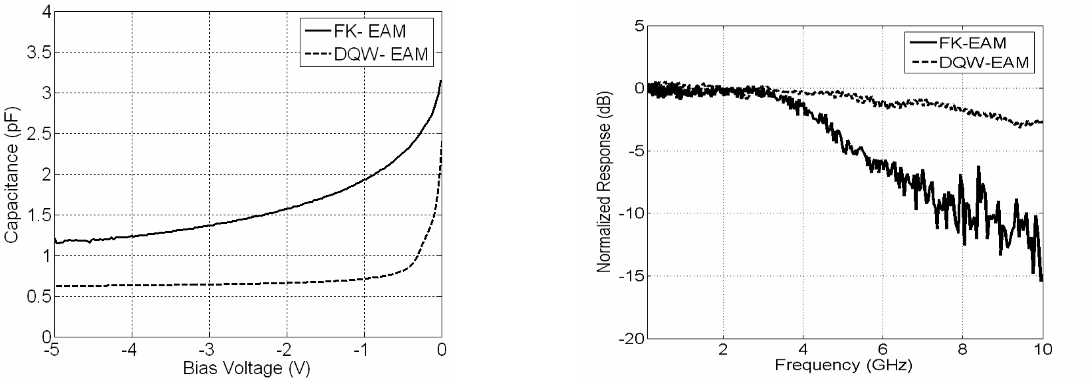

(a) (b)

Fig. 15 (a) Capacitance versus reverse bias for 40µm by 40µm capacitors fabricated from both bulk FK material and DQW material. (b) Normalized frequency response of 400µm long FK EAM and dual QW EAM.

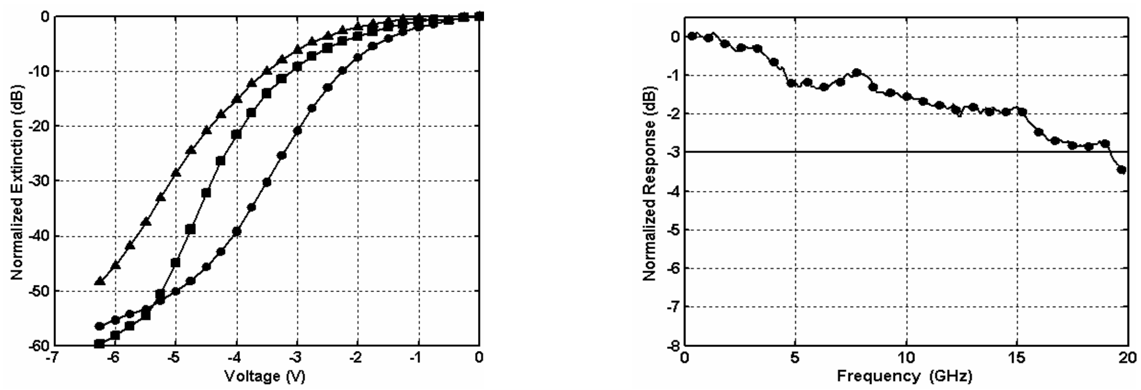

(a) (b)

Fig. 16 (a) DC Extinction of a 175 µm EAM fabricated with QWI for wavelengths of 1558 nm (circles), 1570 nm (squares), and 1580 nm (triangles). And (b) electrical to optical frequency response of the same EAM. The circular markers represent every 30th data point.

long dual QW EAM demonstrating 10 GHz of 3 dB bandwidth, which is a factor of 2 better than the FK EAM response shown on the same plot. Thus, with the dual QW platform we have demonstrated a 2X improvement in EAM efficiency and bandwidth without any degradation to the laser performance or additional fabrication steps than those associated with the offset QW platform.

6.2 SG-DBR /EAM 10 Gb/s Transmitter Fabricated with QWI

With the use of QWI, we have for the first time, fabricated a widely-tunable transmitter demonstrating negative chirp characteristics at 10 Gb/s over its entire tuning range[22] .The transmitter device consists of an SG-DBR laser followed by an EAM. The SG-DBR laser demonstrated a threshold current of 13mA, with an output power of 10mW at a gain section current of 100mA. At this operating point, a side mode suppression ratio (SMSR) greater than 35 dB was achieved. The EAM (175 µm) demonstrated over 40 dB of DC extinction for wavelengths of 1558, 1570, and 1580 nm, with efficiencies greater than 20 dB/Volt as shown in Fig. 16a. The efficient extinction properties are due to the combination of the centered quantum well design and the intermixing process that allows for precise placement of the modulator band edge. The 3dB bandwidth, shown in Fig. 16b, of the same modulator was greater than 19 GHz. Eye diagrams, shown in Fig. 17a, were taken at wavelengths of 1558 nm, 1564 nm, 1571 nm, and 1578 nm with DC biases ranging from -2.1 to -3.8 V and peak to peak voltage swings ranging from 2.2 V to 3.4 V. Greater than 10 dB extinction was achieved at all wavelengths.

Transmission experiments at 10 Gb/s were performed using a non-return to zero (NRZ) pseudo-random-bit-sequence (PRBS) of 2^{31}-1 through Corning SMF-28 fiber. BER curves through 25, 50, and 75 km of fiber at a wavelength of

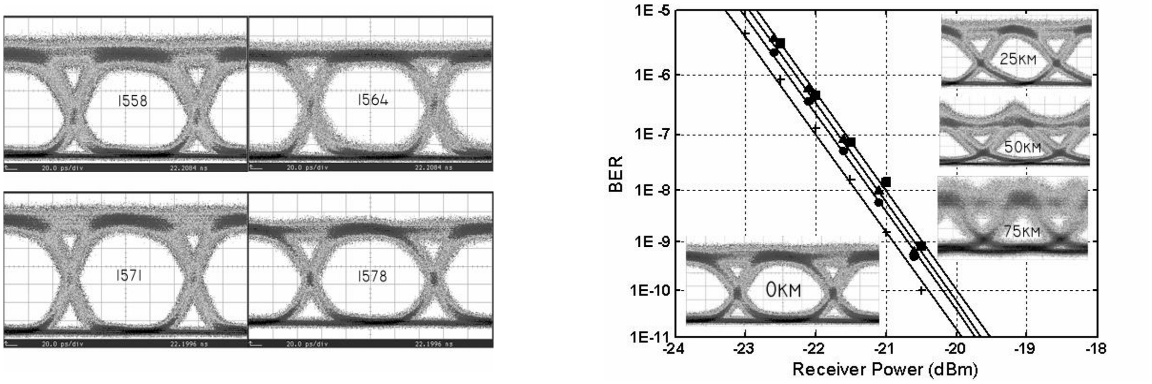

(a) (b)

Fig. 17 (a) 10Gb/s back-to-back eye diagrams from transmitter at wavelengths of 1558 nm, 1564 nm, 1571 nm, and 1578 nm and (b) BER curves/eye diagrams for back-to-back (cross), and transmission through 25 km (circles), 50 km (triangles), and 75 km (squares) of fiber.

1564 nm are shown in Fig. 17b. The EAM was biased at -3.5 V with a 2.0 V peak-to-peak swing. Error-free operation was achieved through 75km of fiber with a power penalty of less than 0.5 dB. The low power penalty transmission is indicative of negative chirp operation, which was confirmed with further testing[20]. The shaping of the eye diagrams due to dispersion is clearly seen in the insets of Fig. 17b where the optical eye diagrams are shown after transmission through fiber.

6.3 High Saturation Power SOAs and Photodiodes Fabricated with QWI and MOCVD Regrowth

The high flexibility QWI and regrowth scheme was used to fabricated high saturation power SOAs and UTC photodiodes. The processing sequence is completely compatible with that used for the fabrication of the SG-DBR/EAM transmitter presented in the previous section. The ridge waveguide SOA chips were soldered to AlN carriers, wirebonded, and placed on a copper stage cooled to 18˚C for characterization. The three characterized SOA designs used a waveguide width of 5μm. The first two designs employed single section low confinement o-MQWs with lengths of 1000μm and 1500μm and the third design used a dual section scheme containing 150μm high optical confinement c-MQW front-end followed by 1350μm of low optical confinement o-MQW. A continuous wave (CW) 1550 nm light source was fed through a polarization controller to maintain the TE polarization state and coupled into the SOA waveguide using a tapered fiber.

The chip gain versus input power and output power versus input power characteristics are shown for the three SOA types in Fig. 18a and Fig. 18b, respectively. In all figures, the operating electrode current density was 9 kA/cm^2 in the o-MQW regions and 20 kA/cm^2 in the c-MQW regions. As can be seen in the figures, a 1000μm long single section o-MQW device provides 6 dB of gain with a saturation output power of over 20 dBm while a 1500μm long single section device provides over 9 dB of chip gain with a saturation output power of 19.5 dBm. By placing a 150μm c-MQW high gain section in front of a 1350μm o-MQW section, the device gain is increased to nearly 15 dB while maintaining a saturation output power of over 19 dBm at 1550nm. Over 13.5 dB of gain was maintained for wavelengths from 1530 to 1560nm.

UTC photodiodes with a waveguide width of 3 μm and length of 25 μm employing an absorber thickness of 50nm and a collector thickness of 150nm were characterized in terms of the internal quantum efficiency, small signal response, and output eye diagrams. The internal quantum efficiency using a 1550nm CW input source was measured to be ~90% in the reverse bias range of 1-4V.

The frequency response of the photodiodes was characterized for various levels of generated photocurrent using a 20 GHz Agilent Lightwave Component Analyzer (LCA). The AlN carrier possessing a matched 50Ω load was probed with ground-signal-ground probes to extract the electrical signal from the photodiode with an effective termination load of

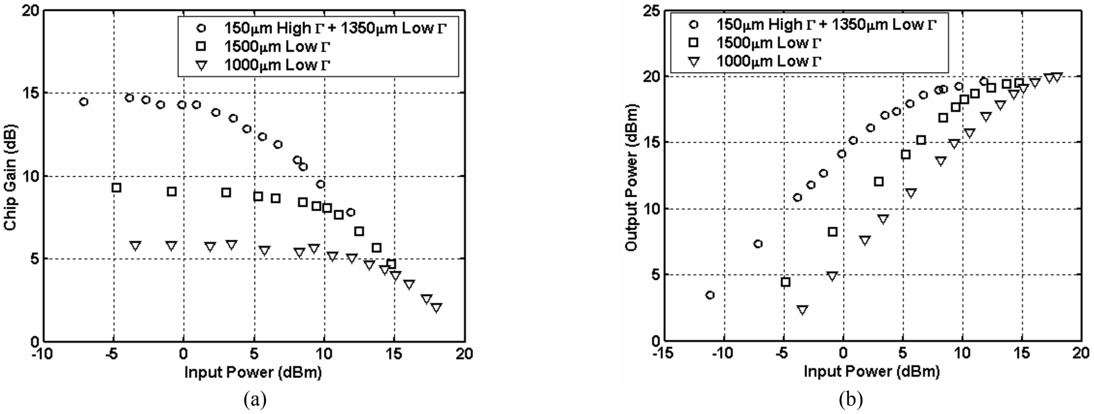

(a) (b)

Fig. 18 (a) Chip gain versus input power and (b) output power versus input power for SOA devices at 1550nm. The applied current density was 9 kA/cm^2 in the low-Γ o-MQW sections and 20 kA/cm^2 in the high-Γ c-MQW sections.

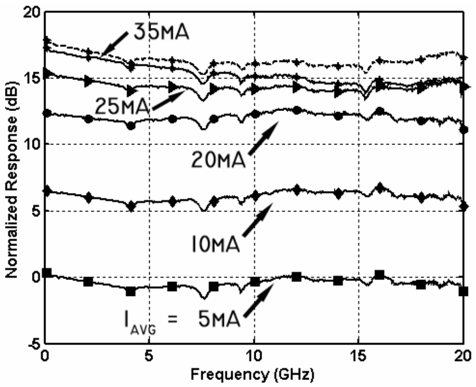

Fig. 19 Optical to electrical response of a 25μm long detector for average photocurrents of 5 (squares), 10 (diamonds), 20 (circles), 25 (triangles), and 35 mA (stars) with a 3V reverse bias and 35 mA at a –4V reverse bias (dashed line).

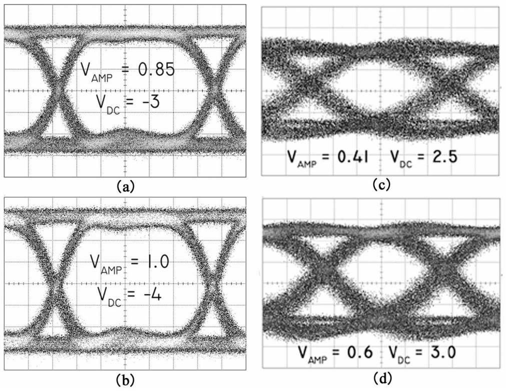

Fig. 20 (a,b) 10 Gb/s and (c,d) 40 Gb/s eye diagrams from a 3 by 25 μm^2 photodetector.

25Ω. The optical to electrical response of a 25 μm long photodiode is shown for various average detected photocurrent levels at a reverse bias of 3V in Fig. 19. The response curves are normalized to the 5mA curve such that they are easily differentiated. As can be seen in the figure, the 20 GHz response demonstrates under 0.5 dB of roll-off with average photocurrents up to 20 mA. At an average photocurrent of 25mA, the roll off is somewhat increased to 0.75 dB and at 35mA the 20 GHz roll-off is increased to slightly over 2 dB. When increasing the reverse bias to 4V at an average photocurrent of 35 mA, the roll-off is decreased to below 1dB.

In Fig. 20a and 20b we present 10 Gb/s eye diagrams taken from a 25 μm long detector at a given input power at reverse biases of 3V and 4V with an effective termination load of 25Ω. The voltage amplitude provided by the photodiode at a reverse bias of 3V was 0.85V and at a reverse bias of 4V it was 1.0V. These amplitudes are indicative of minimum peak currents of 34 and 40 mA, respectively, since the voltage drop was obtained over a 25Ω effective load. In Fig. 20c and 20d we present 40 Gb/s eye diagrams taken from a 25 μm long detector with two different input power levels at a reverse bias of 2.5V and 3.0V. The voltage amplitude of these eyes was measured at 0.41V and 0.6V. As can be seen from the figure, the eye diagrams are open and clear. The 0.6V amplitude provided by the photodiode at 3V is indicative of a minimum peak current of 24mA in the photodiode.

7 CONCLUSION

The monolithic integration of optoelectronic components supporting modern day communication systems will provide solutions at low cost with a reduction of space requirements and device power dissipation. However, as the functionality of the PIC is increased, the challenge of realizing a high performance integrated circuit is great due to the unique characteristics required by the individual components for optimum performance. To meet the increasing performance demands placed upon the PICs, novel integration platforms must be developed such that the design space is increased without significant increase in processing and growth requirements that can raise cost and lower yields.

In this manuscript we have presented two viable integration technologies, which provide the foundation for the monolithic integration of QW EAMs with widely tunable SG-DBR lasers. By growing a blue-shifted MQW in the bulk waveguide below the active MQW in the base structure, etching the active MQW in regions where gain is not required and performing a regrowth of the upper cladding, the dual QW platform requires the same simple processing/growth steps as the well-established offset QW platform with the added flexibility of a second MQW bandedge. By using our implant enhanced QWI scheme, any number of MQW band-edges can be realized on the same chip for the fabrication of high-functionality PICs. Furthermore, this method enables the use of a centered MQW active region for maximized modal gain lasers. Through the use of QWI, we have demonstrated the first widely-tunable negative chirp EAM based transmitter.

Building off these foundational platforms for the integration of lasers and QW EAMs, further techniques were demonstrated as a means for the integration of enhanced performance SOAs and photodiodes. Simple waveguide flares and tapers were shown to increase the 1 dB compressed output power of SOAs by 3-4X up to the 16 dBm range and increase the photocurrent handling capabilities of the integrated QW p-i-n photodetectors by over 50%. These flare/taper techniques were employed in a photoreceiver that was monolithically integrated with a widely-tunable SG-DBR/QW EAM transmitter using the dual QW platform for the realization of a 10 Gb/s PD-WC[33]. The transmitters simultaneously demonstrated high output powers, high side-mode suppression, and wide-tunability. The integrated QW EAMs possessed over 2X the efficiency and bandwidth of equal length FK devices fabricated on the offset QW platform.

For further increased SOA and photodetector performance we have developed a novel QWI and MOCVD regrowth scheme for the integration of low optical confinement factor SOAs and UTC photodiodes with high gain lasers and QW EAMs. Using this scheme, SOAs were fabricated that facilitate saturation output powers in the 19-20 dBm range while providing ~15 dB of gain. The fabricated UTC photodiodes showed excellent photocurrent handling capabilities with a 25 μm by 3 μm detector demonstrating only minimal bandwidth degradation out to 20 GHz while driving 35 mA of average photocurrent. As these components have been developed using processing and growth schemes completely compatible with that of the SG-DBR/QW EAM transmitter, current work is focused on the integration of widely-tunable SG-DBR lasers, negative chirp QW EAMs, high saturation power SOAs, and high saturation power UTC photodiodes.

8 REFERENCES

[1] G. P. Agrawal, Fiber Optic Communication Systems, New York: John Wiley & Sons, Inc., 1997, pp. 3-7.

[2] M. Hatcher and M. Libby, “Foundry model could be key to InP industry future,” *Compound Semiconductor,*Vol. 11 no. 7 pp17-19. Aug. 2005.

[3] M. Sysak, J. Barton, L. Johansson, J. Raring, E. Skogen, M. Mašanović, D. Blumenthal, and L. Coldren, “Single Chip Wavelength Conversion using a Photocurrent Driven (PD) EA Modulator integrated with a Widely Tunable Sampled Grating DBR (SGDBR) Laser,” IEEE Photon. Technol. Lett., vol. 16, pp. 2093-2095, 2004.

[4] J. Raring, E. Skogen, L. Johansson, M. Sysak, J. Barton, Milan L. Mašanović, and L. Coldren, “Quantum Well Intermixing for Monolithic Integration: A Demonstration of Novel Widely-Tunable 10Gb/s Transmitters and Wavelength Converters,” Integrated Photonics Research Conf., San Francisco 2004.

[5] E. Skogen, J. Raring, J. Barton, S. DenBaars, and L. Coldren, “Post-Growth Control of the Quantum-Well Band Edge for the Monolithic Integration of Widely-Tunable Lasers and Electroabsorption Modulators,” IEEE J. Sel. Topics in Quantum Electron., vol. 9, pp. 1183-1190, September/October.

[6] K. Morito, S. Tanaka, S. Tomabechi, and A. Kuramata, “A broadband MQW semiconductor optical amplifier with high saturation output power and low noise figure”. Semiconductor Optical Amplifiers and their Applications Meeting. PD1-1. San Francisco, CA June 30 2004

[7] T. Ishibashi, T. Furuta, H. Fushimi, and H. Ito, “Photoresponse characteristics of uni-traveling-carrier photodiodes” Invited paper. Proceedings of SPIE Vol. 4283 (2001).

[8] J. Binsma, P. Thijs, T. VanDongen, E. Jansen, A. Staring, G. VanDenHoven, and L. Tiemeijer, “Characterization of Butt-Joint InGaAsP Waveguides and Their Application to 1310 nm DBR-Type MQW Ganin-Clamped Semiconductor Optical Amplifiers,” IEICE Trans. Electron., vol. E80-C, pp. 675-681, 1997.

[9] M. Aoki, M. Suzuki, H. Sano, T. Kawano, T. Ido, T. Taniwatari, K. Uomi, and A. Takai, “InGaAs/InGaAsP MQW Electroabsorption Mofulator Integrated with a DFB Laser Fabricated by Band-Gap Energy Control Selective Area MOCVD,” IEEE J Quantum Electron., vol. 29, pp. 2088-2096, 1993.

[10] B. Mason, G. Fish, S. DenBaars, and L. Coldren, “Ridge Waveguide Sampled Grating DBR Lasers with 22-nm Quasi-Continuous Tuning Range,” IEEE Photon. Technol. Lett., vol. 10, pp. 1211-1213, 1998.

[11] M.K. Chin, “Comparative Analysis of the performance analysis of Franz Keldysh effect and quantum confined stark effect electroabsorption waveguide modulators,” IEE Proc. Optoelectron, vol. 142, pp. no. 2. pp. 109-114. 1995

[12] B. Mason, G. Fish, S. DenBaars, and L. Coldren, “Widely Tunable Sampled Grating DBR Lasers with Integrated Electroabsorption Modulator,” IEEE Photon. Technol. Lett., vol. 11, pp. 638-640, 1999.

[13] B. Mason, J. Barton, G. Fish, and L. Coldren, “Design of Sampled Grating DBR Lasers with Integrated Semiconductor Optical Amplifiers,” IEEE Photon. Technol. Lett., vol. 12, pp. 762-764, 2000.

[14] J. Barton, M. Mašanovic, E. Skogen, and L. Coldren, “Widely-Tunable High-Speed Transmitters Using Integrated SGDBRs and Mach-Zehnder Modulators,” IEEE J. Sel. Topics in Quantum Electron., vol. 9, pp. 1113-1117, September/October, 2003.

[15] A. Tauke-Pedretti, M. Dummer, J.S. Barton, M.N. Sysak, J.W. Raring, and L.A. Coldren, “High Saturation Power and High Gain Integrated Photoreceivers,” IEEE Photon. Technol. Lett., vol. 17, pp. 2167-2169, 2005.

[16] J.S. Barton, A. Tauke-Pedretti, M. Dummer, M.N. Sysak, M.L. Mašanović, J.W. Raring, E.J. Skogen, and L.A. Coldren, “10Gbit/s Wavelength Conversion Using a Widely-Tunable Series Push-Pull Photocurrent-Driven Transmitter,” IEEE Photon. Technol. Lett., vol. 17, pp. 1902-1904, 2005.

[17] S. McDougall, O. Kowalski, C. Hamilton, F. Camacho, B. Qiu, M. Ke, R. De La Rue, A. Bryce, and J. Marsh, "Monolithic Integration via a Universal Damage Enhanced Quantum-Well Intermixing Technique," IEEE J. Sel. Topics in Quantum Electron., vol. 4, pp. 636-646, 1998.

[18] S. Charbonneau, E. Kotels, P. Poole, J. He, G. Aers, J. Haysom, M. Buchanan, Y. Feng, A. Delage, F. Yang, M. Davies, R. Goldberg, P. Piva, and I. Mitchell, "Photonic Integrated Circuits Fabricated Using Ion Implantation," IEEE J. Sel. Topics in Quantum Electron., vol. 4, pp. 772-793, 1998.

[19] D. Hofstetter, B. Maisenholder, and H. Zappe, "Quantum-Well Intermixing for Fabrication of Lasers and Photonic Integrated Circutis," IEEE J. Sel. Topics in Quantum Electron., vol. 4, pp. 794-802, 1998.

[20] G. B. Morrison, J.W. Raring, E.J. Skogen, C.S. Wang, and L.A. Coldren, Photocurrent Spectroscopy Analysis of Widely Tunable Negative-Chirp Quantum Well Intermixed Laser-Modulator Transmitters. Applied Physics Letts. vol. 86, Feb, 2005.

[21] C. Wang, E. Skogen, J. Raring, G. Morrison, and L. Coldren, "Short-Cavity 1.55μm DBR Lasers Integrated with High-Speed EAM Modulators," Proc. IEEE International Semiconductor Laser Conf., paper no. WB1, Matsue-shi, Japan (Sept. 21-25, 2004).

[22] J. Raring, E. Skogen, L. Johansson, M. Sysak, S. Denbaars, and L. Coldren: " Widely-Tunable Negative-Chirp SG-DBR Laser/EA-Modulated Transmitter", IEEE Journal of Lightwave Technology. vol. 23 no.1, pp. 80-86, Jan. 2005

[23] V. Lal, M. L. Masanovic, E. J. Skogen, J. W. Raring, J. A. Summers, L. A. Coldren, and D. J. Blumenthal, "Quantum Well Intermixed Monolithically-Integrated Widely-Tunable All-Optical Wavelength Converter Operating at 10Gbps Across the C-band," IEEE Photon. Technol. Lett., vol. 17, pp. 1689-1691, 2005.

[24] E. Skogen, J. Raring, G. Morrison, C. Wang, V. Lal, M. Masonovic, and L. Coldren, "Monolithically Integrated Active Components: A Quantum Well Intermixing Approach," IEEE J. Sel. Topics in Quantum Electron., vol. 11, pp. 343-355, March/April, 2005

[25] L. Coldren, and S. Corzine, Diode Lasers and Photonic Integrated Circuits, New York: John Wiley & Sons, Inc., 1995, pp. 456.

[26] S. Demiguel, L. Giraudet, L. Joulaud, J. Decobert, F. Blache, V. Coupe, F. Jorge. P. Pagnod-Rosiaux, E. Boucherez, F. Devaux. "Evanescently Coupled Photodiodes Integrating a Double Stage Taper for 40Gb/s Applications – Compared Performance With Side-Illuminated Photodiodes" IEEE J. Lightwave Technol.., vol. 20, no. 12, pp. 2004 2014. Dec. 2002.

[27] T. W. Berg and J. Mork, "Saturation and Noise Properties of Quantum-Dot Optical Amplifiers" .IEEE J. Quantum Electronics. Vol. 40 NO. 11, November 2004.

[28] P. W. Juodawlkis, J. J. Plant, R. K. Huang, L. J Missaggia, and J. P. "High Power 1.5μm InGaAsP-InP Slab-Coupled Optical Waveguide Amplifier," IEEE Photon. Technol. Letts. vol. 17, Feb, 2005.

[29] T H. Wood, J. Z. Pastalan, C. A. Burrus, Jr., B. C. Johnson, B. I. Miller, J. L. deMiguel, U. Koren, and M. G. Young "Electric field screening by photogenerated holes in multiple quantum wells: A new mechanism for absorption saturation" Applied Physics Letts. vol. 57, no. 11, pp. 1081-1083 Sept. 1990.

[30] E. Skogen, J. Raring, S. DenBaars, and L. Coldren, "Integration of High-Gain and High-Saturation Power Active Regions using Quantum Well Intermixing and Offset-Quantum Well Regrowth," Electron. Lett., Vol. 40, pp. 993-94, 2004.

[31] J. Raring, E. Skogen, S. Denbaars, and L. Coldren: "A Study of Regrowth Interface and Material Quality for a Novel InP Based Architecture," Journal of Crystal Growth. vol. 273/1-2 pp. 26-37 Dec. 2004

[32] J. S. Barton, A. Tauke-Pedretti, M. Dummer, M. N. Sysak, J. W. Raring, L. A. Coldren, "Field modulated wavelength conversion , *Invited,* 6124 -42. San Jose, CA, January 21-26, 2006